Journal of Physics and Chemistry of Solids 167 (2022) 110721

Contents lists available at ScienceDirect

Journal of Physics and Chemistry of Solids

journal homepage: www.elsevier.com/locate/jpcs

Enhancement of electrical conductivity to metallization of $Mn_{3-x}Fe_xO_4$ spinel and postspinel with elevating pressure

HPSTAR 1458-2022

Takamitsu Yamanaka, Pro. Doc [a,b,*], Saqib Rahman, Dr. [a], Yuki Nakamoto, Dr. [c], Takanori Hattori, Dr. [d], Bo Gyu Jang, Dr. [a], Duck Young Kim, Prof. Dr. [a], Ho-kwang Mao, Dr. [a]

[a] Center for High Pressure Science & Technology Advanced Research (HPSTAR), 1690 Cailun Rd., Pudong, Shanghai, 201-2003, PR China
[b] Department Earth and Space Science, Graduate School of Science, Osaka University, 1-1 Machikaneyama Toyonaka, Osaka, 560-0043, Japan
[c] Center of Quantum Science and Technology under Extreme Conditions, Osaka University, 1-1 Machikaneyama Toyonaka, Osaka, 560-0043, Japan
[d] Materials and Life Science Division, Japan Proton Accelerator Research Complex (J-PARC), 2-4 Sirakata Tokaimura, Naka-gun, Ibaraki, 319-1195, Japan

ARTICLE INFO

Keywords:
$Mn_{3-x}Fe_xO_4$
Magnetic properties
High pressure
Neutron diffraction
Synchrotron X-ray mössbauer spectroscopy
Electrical resistivity
Metallization

ABSTRACT

Electrical conductivity enhancement from semiconductor to metallization in $Mn_{3-x}Fe_xO_4$ postspinel under extreme conditions is discussed herein. Neutron diffraction experiments have allowed precise analysis of the $Mn_{3-x}Fe_xO_4$ structure by virtue of the significant difference in coherent scattering lengths between Mn (−3.73 fm) and Fe (9.54 fm). An $Mn_{3-x}Fe_xO_4$ spinel solid solution transforms into an orthorhombic postspinel phase. Neutron diffraction studies have proved that cubic $MnFe_2O_4$ spinel and tetragonal Mn_2FeO_4 transform into a high-pressure postspinel structure ($CaMn_2O_4$-type marokite) above pressures of 18 GPa and 14 GPa, respectively. The transition pressure decreases with increasing Mn content.

Synchrotron X-ray Mössbauer experiments have revealed the effects of high pressures on the distribution of Fe^{2+} and Fe^{3+} at the tetrahedral and octahedral sites in the spinel structure. $MnFe_2O_4$ and Mn_2FeO_4 are ferrimagnetic under ambient conditions, and they show sextet spectral features with hyperfine structure elicited by internal magnetic fields. The high-pressure postspinel polymorph shows paramagnetic character.

Electron hopping persists as the charge-transport mode. The temperature dependence of resistivity indicates that the spinel phases show semiconductor properties. Electrical conduction is derived from electron hopping between cations at the tetrahedral (A) and octahedral (B) sites. A shortened B–B distance promotes higher conduction during compression and greater electron mobility between adjacent B cations. The occupancies of Fe^{2+} and Fe^{3+} at the B sites of $MnFe_2O_4$ are much higher than in the case of Mn_2FeO_4. The high-pressure postspinel polymorph of transforms into a phase with metallic-like character due to band conduction in the high-pressure region. Theoretical approaches have revealed the densities of state of these manganese ferrites. To verify the metallic behavior of postspinel Mn_2FeO_4 under high pressures, we have applied a combined approach of density functional theory and dynamical mean field theory. The spectral function clearly shows metallic character. Fe d orbitals are strongly renormalized compared to Mn d orbitals.

1. Introduction

Solid solutions of $Mn_{3-x}Fe_xO_4$ spinels have a magnetic structure with two-dimensional triangular Yafet–Kittel spin configuration [1–3]. Disorder in the cation distribution between A (tetrahedral) and B (octahedral) sites in AB_2O_4 spinels has a great influence on magnetic properties, such as saturation magnetization, exchange coupling, and ferrimagnetic ordering temperature. The cation distribution depends on electronic configuration, electrostatic energies, and polarization effects, and defines the magnetic properties of the ferrites and the manifestation of non-collinear spin structures in Yafet–Kittel spin configurations. Structural analyses of the solid solutions obtained from Fe_3O_4 and Mn_3O_4 have been conducted by thermal neutron diffraction [4,5], because these are the most fundamental ferrite substances for industrial materials composed of mixed-charge cations in the A and B sites.

Magnetite undergoes a phase transition to a high-pressure (HP) form,

* Corresponding author. Center for High Pressure Science & Technology Advanced Research (HPSTAR), 1690 Cailun Rd., Pudong, Shanghai, 201-2003, PR China.
E-mail addresses: t.yamanaka@cap.ocn.ne.jp, takamitsu.yamanaka@hpstar.ac.cn (T. Yamanaka), saqib.rahman@hpstar.ac.cn (S. Rahman), nakamoto@stec.es.osaka-u.ac.jp (Y. Nakamoto), hattori.takanori@jaea.go.jp (T. Hattori), bogyu.jang@hpstar.ac.cn (B.G. Jang), duckyoung.kim@hpstar.ac.cn (D.Y. Kim), maohk@hpstar.ac.cn (H.-k. Mao).

https://doi.org/10.1016/j.jpcs.2022.110721
Received 15 December 2021; Received in revised form 30 March 2022; Accepted 31 March 2022
Available online 22 April 2022

denoted as h-Fe_3O_4. The stability field and crystal structure of h-Fe_3O_4 initially implied that it had a $CaTi_2O_4$-type structure with space group *Bbmm* (*Cmcm*) above 25 GPa, but this was later refined to $CaMn_2O_4$ (*Pbcm*). There have been several X-ray powder diffraction studies of magnetite under HP conditions [6–11].

Electrical metallization of spinel compounds under high pressure has been characterized by electrical resistivity measurements. The Verwey transition temperature of Fe_3O_4 decreases non-linearly with increasing pressure [12]. A steep change in its resistivity at the Verwey transition temperature is observed at pressures below 6.5 GPa, and it exhibits metallic behavior above 8 GPa. The pressure dependence of the electrical resistivity of magnetite has been measured, and metallicity arose after suppression of the Verwey transition around 20 GPa. The concomitant enhancement of electrical conductivity is caused by the structural transformation to the high-pressure phase [13].

Under high-pressure and high-temperature conditions, the $Mn_{3-x}Fe_xO_4$ spinel structure transforms to a high-pressure phase of orthorhombic $CaMn_2O_4$-type structure. The transition pressures of the $Mn_{3-x}Fe_xO_4$ solid solution at ambient temperature are: Fe_3O_4 at 21.8 GPa, $MnFe_2O_4$ at 18.4 GPa, and Mn_3O_4 at 10 GPa [6,14,15].

The electrical properties of spinels have been characterized by first-principles calculations. $ZnMn_2O_4$ transforms to an HP phase with a $CaMn_2O_4$ (marokite)-type structure (space group *Pbcm*) at 15.9 GPa. Another HP polymorph is proposed to have an $MgAl_2S_4$ inverted spinel-type structure (space group *Imma*) [16]. Raman spectroscopy and electrical transport measurements of $Zn_{0.2}Mg_{0.8}Fe_2O_4$ have shown that the cubic spinel undergoes a pressure-induced transition to an orthorhombic phase ($CaTi_2O_4$-type *Bbmm*) at 21 GPa. The onset of the Mott insulator–metal transition around 20 GPa was attributed to a spin-crossover mechanism, which led to collapse of the Fe^{3+} magnetic moment. The orthorhombic HP phase was found to have higher conductivity than that of the cubic phase. The pressure dependence of the conductivity supported the metallic nature of the HP phase [17]. $Co_{0.5}Mg_{0.5}Cr_2O_4$ showed a cubic-to-tetragonal phase transition, and the temperature dependences of the resistivity at different pressures were determined from the wide band gap of the semiconductor nature with different activation energy, suggesting a semiconductor-to-metallic transition [18]. The $MnFe_2O_4$ spinel undergoes a phase transition to postspinel at about 18.4 GPa to form a denser paramagnetic $CaMn_2O_4$-type polymorph [19]. Our previous Raman spectroscopic studies and powder X-ray diffraction studies of various postspinels have indicated orthorhombic phases with $CaFe_2O_4$-type (*Pmma*), $CaTi_2O_4$-type (*Cmcm*), and $CaMn_2O_4$-type (*Pbcm*) structures as high-pressure polymorphs (Yamanaka et al., 2008). Transformations of the oxide spinels are summarized in **Supplementary Information File 1**.

$Mn_{3-x}Fe_xO_4$ solid solutions are ferrimagnetic and can be characterized as semiconductors. The classical band structure of solid-state physics predicts the Fermi level to lie in a band region within the conduction band for metals. Metallic behavior is seen for compounds with partially filled bands under high pressure. The interaction-driven insulating state is referred to as a Mott insulator. The distribution of 3d-electron Mn and Fe atoms at the A and B sites in $MnFe_2O_4$ and Mn_2FeO_4 at high pressure has a strong influence on the electrical conductivities of these spinels. This is due to electron-electron correlation.

In the present study, we have focused on the enhancement of electrical conductivity from semiconductor to metal in $Mn_{3-x}Fe_xO_4$ spinel and postspinel with increasing pressure. To assess this, neutron diffraction at high pressure and high temperature has been conducted, and the precise cation distribution has been elucidated by making use of the significant difference in coherent scattering lengths between Mn and Fe. Furthermore, Fe^{2+} and Fe^{3+} distributions have been clarified by synchrotron X-ray Mössbauer experiments at increasing pressure.

2. Experimental

2.1. Sample preparation

In $Mn_{3-x}Fe_xO_4$ solid solutions, Fe_3O_4 and $MnFe_2O_4$ are cubic. However, Mn-rich phases of Mn_2FeO_4 and Mn_3O_4 (tetragonal under ambient conditions) are observed by high-temperature X-ray diffraction analysis. The cubic phase contains more than 54 mol.% Fe_3O_4, but a tetragonal phase with lower Fe_3O_4 content is found in the solid solutions [20]. In the present study, $MnFe_2O_4$ (33 mol.%) and $MnFe_2O_4$ (66 mol.%) were synthesized. These adopt cubic and tetragonal phases, respectively, under ambient conditions.

Powder samples of $MnFe_2O_4$ and Mn_2FeO_4 were prepared by solid-solid reaction at ambient pressure. To prepare samples for synchrotron X-ray Mössbauer experiments, ^{57}Fe-isotope-enriched samples with 30% ^{57}Fe content were prepared with authentic reagent grade Fe_2O_3 and MnO_2 specimens. To prepare stoichiometric samples, special care was taken to control the partial pressure of oxygen ($Po_2 = 10^{-4}$–10^{-8}), using a H_2/CO_2 gas mixture. The samples were synthesized at 1300 °C in an alumina crucible in the gas flow for 48 h and then pulverized after quenching. This procedure was repeated three times to produce a homogeneous sample. The chemical compositions of the synthesized samples were analyzed with an electron probe microanalyzer (EPMA, JEOL JXA-8530F) at the University of Tokyo using well-characterized natural and synthetic standards. The homogeneity of the samples was examined by acquiring back-scattered electron images of Fe and Mn X-ray mappings, along with scanning electron microscopy (SEM) and secondary electron images (the latter formed by detecting secondary electrons generated from excitation of the constituent atoms by inelastic scattering of the incident (primary) electrons in a specimen). Chemical disorder significantly influences electrical resistivity and magnetic susceptibility. Neither trace elements nor impurities were found in the samples. More detailed information about the sample preparation can be found in a previous paper [21].

2.2. High-pressure powder synchrotron diffraction

Precise measurements of the transition pressures and hysteresis of $Mn_{3-x}Fe_xO_4$ solid solutions were performed by synchrotron X-ray powder diffraction experiments at high pressures up to 40 GPa at room temperature. A symmetrical diamond anvil cell with 350 μm diameter culets was used. A rhenium gasket was pre-indented from 200 μm to 80 μm. Pressure measurement was carried out by the ruby fluorescence method [22]. In experiments at up to 15 GPa, the sample was placed in the gasket hole of diameter 125 μm, together with the pressure-transmitting medium of ethanol/methanol/water mixture. Above this pressure, no pressure-transmitting medium was used, and the sample was placed under non-hydrostatic conditions. In order to overcome deviatoric stress, the sample was kept at the requisite pressure for annealing for about 20 min. The sample had a fine grain size, as it was taken from the floating particles in the alcoholic medium to avoid spotty diffraction powder rings. Angle-dispersive diffraction studies were undertaken using synchrotron radiation at the Photon Factory (KEK), Tsukuba, operating at 2.5 GeV and 360 mA. A flat cassette-type imaging plate detector was employed at the undulator beam line BL-13A using a monochromatic beam of about 30 keV. The exposure time for each diffraction pattern was about 20 min, with a beam of 15–45 μm collimated through focusing mirrors. A precise profile analysis in the range $2\theta = 5$–$15°$ was also carried out using a narrow collimator of 15 μm. The diffraction patterns were integrated using Fit2D software [23]. Rietveld refinement analyses were carried out using Rietan2000 software [24].

2.3. High-pressure electrical resistivity measurements

For electrical resistivity measurements under pressure, spring-steel with a 250 μm hole was used to constrain the sample between

diamonds. The gasket was electrically insulated by coating with an MgO-epoxy composite mixed in a 3:1 ratio prior to sample loading. The pre-indented and drilled gasket was filled with MgO powder and compressed, providing additional insulation between the gasket and the sample. A sample layer was placed on top of the MgO, and two 25 μm diameter platinum leads were placed on top of the sample powder. A small amount of ruby chips placed between the leads was used to measure pressure on the ruby fluorescence pressure scale. Pressure gradients were observed at several spots between the leads.

Our lowest-pressure data were collected at 0.25 GPa; this procedure ensured that the sample was in good contact with the leads. Resistances were measured during both compression and decompression by means of a digital multimeter. Measurements were reproducible to within 1 Ω, or better than 4% in resistivity for our highest-pressure measurements; at lower pressures (below 5 GPa), measurements were reproducible to within 0.5%. The resistance of the sample was calculated by subtracting the resistance measured through a lead from the resistance measured across the sample. Electrical resistances measured across the samples were in the range from 187 Ω to 18 Ω, while characteristic resistances of the wires were 10 Ω ideally. The wiring configuration allowed the sample to be measured across two of the four leads, and the measured resistance was compared with that across the other two leads. The resistances of both wires were also measured. Full details of the experimental procedure can be found in our previous paper [13].

To calculate the resistivity of the samples (r), we used the following relationship:

$$r=(R\mathrm{W}t)/L \tag{1}$$

where R is the electrical resistance, W is the length of lead overlap (the segment of the two wires between which the current flows), L is the distance between the leads, and t is the thickness. W was measured as 25 ± 10 μm, L was 125 ± 5 μm, and t was estimated as 10 ± 2 μm based on optical inspection of the samples following decompression.

Sample geometry remained constant throughout the studied pressure range; the geometry (particularly the thickness) was the primary source of error in these measurements, contributing to an overall uncertainty of 20%. The electrical resistance of this sample was measured at pressures up to 40 GPa at ambient temperature.

2.4. Neutron diffraction experiments at high pressure

We investigated the magnetic structures of $MnFe_2O_4$ and Mn_2FeO_4 by spallation neutron time-of-flight (TOF) scattering under simultaneous high-pressure and high-temperature conditions. The X-ray structure analysis of $Mn_{3-x}Fe_xO_4$ was subject to ambiguity, because the X-ray scattering factors of Fe (26) and Mn (25) are extremely similar. However, neutron diffraction analysis could precisely characterize $Mn_{3-x}Fe_xO_4$ by virtue of the significant difference in coherent scattering lengths between Mn (−3.73 fm) and Fe (9.54 fm).

For experiments at pressures up to 30 GPa, we used a Paris–Edinburgh (PE) press (VX4) operated at room temperature [25], as well as a six-axis multi-anvil press, ATSUHIME at PLANET J-PARC [26], for experiments at pressures up to 10 GPa and temperatures up to 1200 °C. The temperature dependence of the structure transition of the solid solution at various pressures was determined using an ATSUHIME high-pressure apparatus.

We performed Rietveld analysis of neutron diffraction data to refine the magnetic structure. The analysis was conducted using the program GSAS [27,28]. The magnetic structure factor F_N(h) for neutron diffraction is expressed as:

$$F_N(h_\mathrm{k}) = \Sigma\gamma_j b_{cj} T_j \, exp\ |2\pi i(hx_j + ky_j + lz_j)| \tag{2}$$

where T_j is the temperature factor of the j th atom, γ indicates the γ-factor of the nuclear magneton ($\gamma = 1.913$), and b is the scattering length ($b_{\mathrm{Mn}} = -3.73$ fm, $b_{\mathrm{Fe}} = 9.54$ fm).

The magnetic scattering factor $F_M(\boldsymbol{h})$ is given by:

$$\mathrm{FM(hi)} = \gamma \mathrm{e}^2 \Big/ 2mc^2 \sqrt{1 - <\cos^2\eta>}\, X f(h_k) \sum \gamma_j b_{cj} T_j \exp\left|2\pi i\left(hx_j + ky_j + lz_j\right)\right| re^2 \Big/ 2mc^2 = 2.696(fm) \tag{3}$$

where γ is the magnetic moment of incident neutron source, and μ is the magnetic moment. The integrated intensity I_o is produced by a combination of magnetic scattering factor and nuclear form factor:

$$I_o = s\,(\boldsymbol{h})A(\boldsymbol{h})L(\boldsymbol{h})m(\boldsymbol{h})\ \{|F_N(\boldsymbol{h})|^2 + |F_M(\boldsymbol{h})|^2\} \tag{4}$$

where s is the scale factor, A is absorption, L is the Lorentz factor, and m is the multiplicity. L (= $d^4\sin\theta$) is quite different from the X-ray diffraction case. The Lorentz factor decreases with Q (momentum tensor) and L, where d is the distance.

In neutron scattering experiments, the flux of neutrons scattered by a sample into a detector is measured as a function of the change in neutron wave vector (Q) and energy (h). The expressions for the scattered neutron flux involve the positions and motions of atomic nuclei or unpaired electron spins.

The goodness-of-fit and the reliability of the refinement are expressed by several parameters, namely χ^2, wR_p, R_p, and R_{p2}. The reliability factor R_p and wR_p are given by:

$$wR_P = [\ (\Sigma_i\ w_i|\ y_i - f_i(x))\ |\ /\ \Sigma_i w_i\ y_i]^{1/2}$$

$$R_F = [\ \Sigma_k\ (|\ F_{k\ obs}\ |\ -\ |\ F_{k\ cal}\ |)/\ \Sigma_k F_{k\ obs}] \tag{5}$$

where $w = 1/\mathrm{r}^2|(\mathrm{F_{obs}})|$; r is the standard deviation of the observed intensity. R (%) indicates the reliability factor ($R = \sum||F_{\mathrm{obs}}|^2 - |F_{\mathrm{cal}}|^2|/\sum|F_{\mathrm{obs}}|^2$).

Least-squares refinement was conducted by the minimization of R:

$$\mathrm{R} = \Sigma\ w(\boldsymbol{h})\{|F_{obc}(\boldsymbol{h})|^2\ -\ |F_{cal}(\boldsymbol{h})|^2\} \tag{6}$$

2.5. Synchrotron X-ray mössbauer experimentes at high pressure

High-pressure X-ray Mössbauer experiments were carried out to determine the electronic charge distribution. We measured the synchrotron X-ray Mössbauer spectra of the $Mn_xFe_{3-x}O_4$ solid solutions at SPring-8 BL-10XU [29] under high pressure using a micro-beam of wavelength of 14.4 keV and a diamond anvil cell (DAC). The cation distribution in $MnFe_2O_4$ was determined from the neutron diffraction data [30,31].

We used the MossA program [32] to analyze Mössbauer spectra and determined the cation distribution and magnetic structure as a function of pressure. The velocity peak positions of the spectra were detected with an error of less than ±0.05 mm/s. The ^{57}Fe spectrum of Fe_2O_3 was taken as the zero velocity as a reference. The internal magnetic fields of the hyperfine-structure spectra were determined with reference to 26.26 T (330 kOe) of ^{57}Fe in the spectrum of Fe_2O_3.

3. Results and discussion

3.1. $Mn_{3-x}Fe_xO_4$ phase relation

Neutron diffraction patterns of Mn_2FeO_4 obtained from heating experiments using ATSUHIME at J-PARC provided insight into the tetragonal-to-cubic transition. Heating and cooling experiments showed how the cubic structure transforms, indicating reversal of the transition and hysteresis in the tetragonal-to-cubic transition. Jahn–Teller effect degradation and appearance in the transitions of Mn_2FeO_4 between tetragonal and cubic spinel forms are shown in the figure in **Supplementary information file 2**. The tetragonal-to-cubic transition of Mn_2FeO_4 occurs at 160 °C at 3 GPa and at 180 °C at 1 GPa according to the temperature dependence of c/a. These experiments proved that the transition temperature decreases with increasing pressure, that is, the P-T boundary between the tetragonal and cubic phases has a negative slope. The lattice distortion is reduced with increasing temperature and finally the lattice constant ratio becomes $c/a = 1$, resulting in transformation to cubic symmetry ($c = a$).

The phase relation of $Mn_{3-x}Fe_xO_4$ at high pressures and the compositional change were thus clarified by neutron diffraction and synchrotron diffraction studies. An example of the neutron diffraction patterns of Mn_2FeO_4 with increasing pressure is presented in Fig. 1. This phase is tetragonal under ambient conditions due to the 3 d^4 electronic configuration of Mn^{3+}. Distortion of the tetragonal phase is induced by the ligand lying along the c-axis. The lattice distortion is reduced with increasing pressure and finally c/a becomes 1, resulting in a transformation to cubic symmetry ($c = a$) above 10 GPa. The Jahn–Teller effect exerts less distortion on the tetragonal lattice upon further compression. The present experiment confirms that an octahedron elongated along the c-axis gradually changes to a regular octahedron with increasing pressure. The cubic phase transforms to an orthorhombic postspinel phase at about 14 GPa.

$MnFe_2O_4$ spinel undergoes a phase transition to an orthorhombic $CaMn_2O_4$-type postspinel at 18 ± 0.2 GPa. The spinel phase is stable up to 18 GPa. A two-phase mixture of the high-pressure polymorphs of postspinel and spinel phases is observed up to 23.5 ± 0.2 GPa. Above 26.1 ± 0.2 GPa, only the postspinel phase is detected. The phase diagram of $Mn_{3-x}Fe_xO_4$ at high pressure is shown in Fig. 1.

The tetragonal-to-cubic transition is driven by interactions between localized orbital electronic states and the crystal lattice. Present Rietveld refinement based on the distortion of the octahedral sites of the tetragonal-cubic structure transition from the bond distance ratio between two and four B–O bonds with increasing pressure. The tetragonal structure is elongated along the c-axis. Mn_2FeO_4 tetragonal spinel is composed of the cooperative Jahn–Teller effect due to Mn^{3+} at octahedral sites. The site symmetry of 0.2/m of the octahedral (B) site in the tetragonal symmetry of $I4_1/amd$ changes to the symmetry of m of the cubic symmetry of $Fd\bar{3}m$.

This site symmetry change is caused by a diminution of the Jahn–-Teller effect with increasing pressure up to 10 GPa.

The TOF neutron diffraction study clarifies the precise Mn and Fe occupancies of the A and B sites in the spinel structure. The site occupancies have a significant effect on electrical conductivity. The magnetic moments of the A and B sites in the $MnFe_2O_4$ and Mn_2FeO_4 spinel structures were also clearly observed. The inverse parameter i of the spinel structure in $(Mn^{2+}_{i}Fe^{3+}_{1-i})[Mn^{3+}_{1-i}Fe^{2+}_{1-i}Fe^{3+}_{2i}]O_4$ could be precisely defined. At high pressure, just before the transition pressures of the respective samples, they more closely adopt the normal spinel structure with $i = 1$. The bond distances at the A and B sites of Mn–O and Fe–O were evaluated through neutron diffraction study. The results of the structure refinements of the spinels and postspinel with increasing pressure are presented in Supplementary Table 1, 2, and 3, respectively. The transition from spinel to postspinel phase has been reported previously [33–35].

In the orthorhombic phases of $CaFe_2O_4$-type (*Pmma*), $CaTi_2O_4$-type (*Cmcm*), and $CaMn_2O_4$-type (*Pbcm*) structures as high-pressure polymorphs, the Ca atoms are located at the eight-fold coordinated M1 sites and the Mn, Ti, and Fe atoms are located at the six-fold coordinated M2 sites. Slight modifications of the octahedra lead to three different structure types, and their mutual interconversions have been revealed by systematic high-pressure experiments up to 80 GPa at ambient

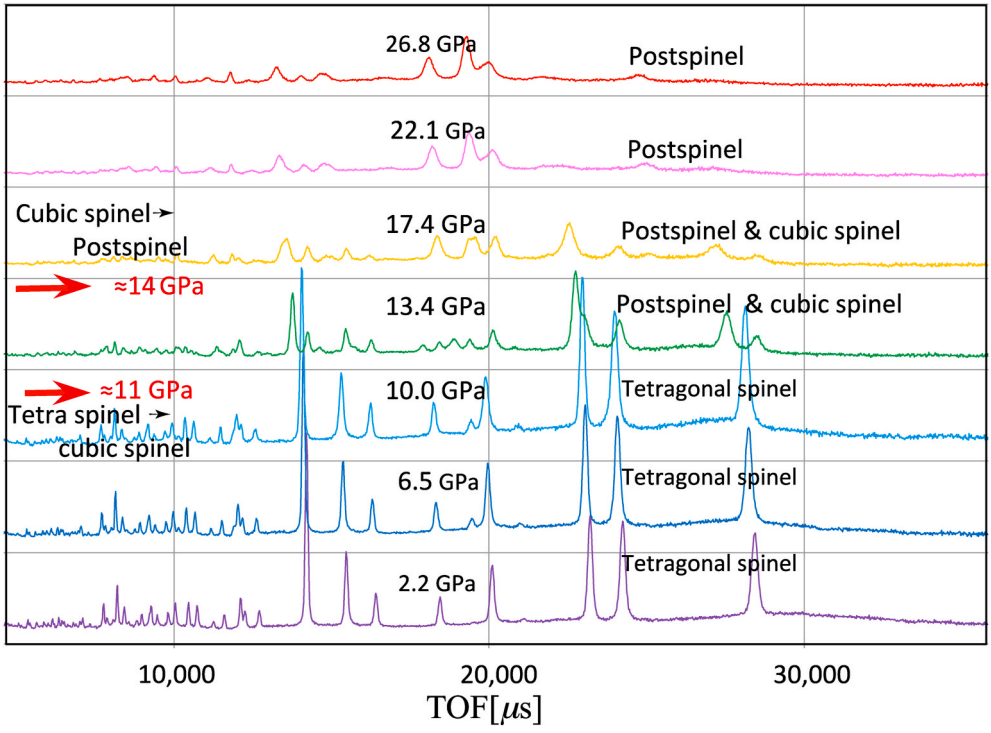

Fig. 1. Powder diffraction pattern of Mn_2FeO_4 observed by neutron diffraction. Tetragonal spinel is transformed to the cubic structure at about 11 GPa. Subsequent transition to the postspinel phase is detected above 14 GPa. The spinel and postspinel coexist in the pressure region up to 18 GPa.

temperature [35]. The postspinel form of $Mn_{3-x}Fe_xO_4$ is of the CaMn$_2$O$_4$-type (*Pbcm*), composed of one M1 (4d) and two M2 (8e) sites. The M1 site (. . m) and M2 sites (1) are extremely deformed, compared with the A site ($\bar{4}$3m) and B site (.3 m) of the cubic spinel structure.

The assignment of Fe^{2+} and Fe^{3+} at the M1 (8-fold) and M2 (6-fold) sites of the postspinel phase was based on synchrotron X-ray Mössbauer experiments. The postspinel structure is composed of edge-sharing octahedra in the plane perpendicular to the *c*-axis, as shown in Supplementary Fig. 1. Two M2 octahedra are linked through a common edge to form a dimer. Such dimers built by octahedral sites are linked in the directions parallel to the *x*- and *y*-axes. The octahedral array in the spinel structure is assembled through corner-sharing of adjacent octahedra.

3.2. Fe^{2+} and Fe^{3+} distribution observed by synchrotron X-ray mössbauer experiments

Structural studies under ambient conditions have indicated that Mn_2FeO_4 has extremely distorted octahedral sites, which stems from a pronounced Jahn–Teller effect of the Mn^{3+} (3 d^4) cation. Insight into electron hopping was needed to discuss the charge distribution in the structure. X-ray and neutron diffraction studies cannot provide information on the charges on the constituent cations. X-ray Mössbauer experiments of Mn_2FeO_4 and $MnFe_2O_4$ spinel and postspinel were performed to elucidate the effects of high pressures up to 30 GPa on the Fe^{2+} and Fe^{3+} distribution. The isomer shift (IS), quadruple splitting (QS), relative intensity, and internal magnetic field (B_{IF}) of each site of $MnFe_2O_4$ spinel are presented in Supplementary Table 4. The data confirm that Mn_2FeO_4 and $MnFe_2O_4$ transform into high-pressure structures above pressures of 18 GPa and 14 GPa, respectively, consistent with the results of X-ray diffraction and neutron diffraction studies (Supplementary Fig. 2).

X-ray Mössbauer spectroscopy proved to be an extremely valuable and indispensable tool for clarifying the cation distribution and magnetic properties of the solid solution of $Mn_{3-x}Fe_xO_4$ ferrite. The Mössbauer spectrum of $MnFe_2O_4$ cubic spinel obtained at 12.5 GPa and 300 K features two hyperfine structures of sextet patterns, as befits ferrimagnetism. The spectra proved the phase to be ferrimagnetic, as shown in Fig. 2 (upper spectrum). The cation distribution can be described as $^{A}(Mn^{2+}_{1-d}Fe^{3+}_{d})^{B}[Mn^{3+}_{d}Fe^{2+}_{d}Fe^{3+}_{2-2d}]O_4$. Under further compression, the Mössbauer spectrum of Mn_2FeO_4 at 17.0 GPa and 300 K features one doublet and one sextet (lower spectrum in Fig. 2). At a little below the spinel-to-postspinel transition pressure, one doublet and one sextet are observed. The doublet indicates Fe^{2+} at octahedral sites (A sites) and the sextet represents a mixture of Fe^{2+} and Fe^{3+}, indicating electron hopping. The hyperfine structure of the Mössbauer spectrum confirms ferrimagnetism.

Two doublets are observed, as shown in Fig. 3. The larger doublet indicates a 6-fold octahedron, and is due to Fe^{3+} at octahedral sites (M2 sites). The other doublet is due to Fe^{2+} in the highly distorted 8-fold large cation site (M1 site). This site is mainly occupied by larger cations.

Cubic spinel $MnFe_2O_4$ and tetragonal Mn_2FeO_4 are ferrimagnetic

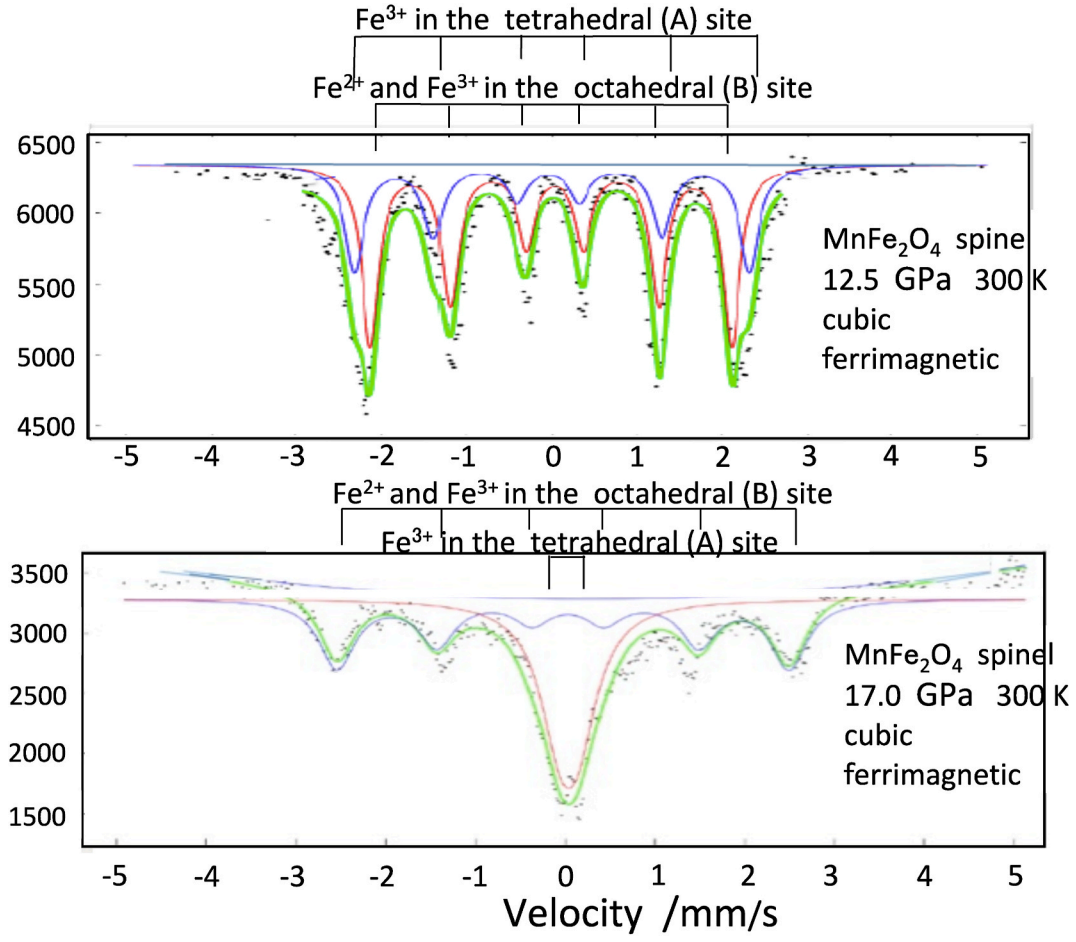

Fig. 2. Mössbauer spectra of $MnFe_2O_4$ cubic spinel. Upper figure: ferrimagnetic cubic phase at 12.5 GPa and 300 K; the spectrum features two hyperfine structures of sextet patterns indicating ferrimagnetism; the cation distribution is described as follows: $^{A}(Mn^{2+}_{1-d}Fe^{3+}_{d})^{B}[Mn^{3+}_{d}Fe^{2+}_{d}Fe^{3+}_{2-2d}]O_4$. Lower figure: ferrimagnetic cubic phase at 17 GPa and 300 K; the spectrum features one doublet attributable to Fe^{3+} at the tetrahedral sites and one sextet attributable to Fe^{2+} and Fe^{3+} at the octahedral sites.

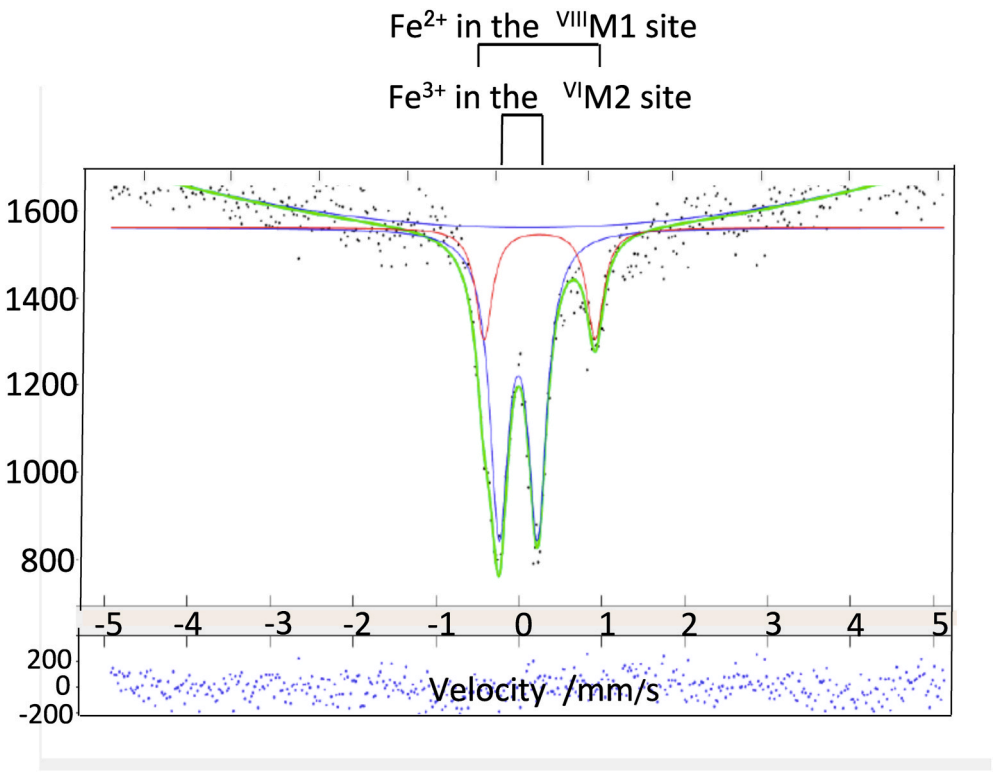

Fig. 3. Mössbauer spectrum of orthorhombic postspinel Mn_2FeO_4 at 18.0 GPa. Two doublets can be seen; the inner larger doublet corresponds to Fe^{3+} at 6-fold octahedral M2 sites; the outer doublet corresponds to Fe^{2+} at highly distorted 8-fold large cation sites (M1 sites). No hyperfine structure can be discerned, showing the postspinel phase to be paramagnetic.

under ambient conditions; they show a hyperfine sextet spectrum elicited by the internal magnetic fields due to Zeeman splitting. However, the postspinel structures of these samples are paramagnetic, which implies that the internal magnetic field is not observed in the high-pressure phase.

The spectrum of postspinel Mn_2FeO_4 at above 18 GPa features two doublets (no more sextets). The inner doublet of higher intensity is assigned to Fe^{3+} at the 6-fold cation M2 site. The outer doublet is assigned to Fe^{2+} at the highly distorted 8-fold large cation M1 site. The area ratio of these two doublets was taken as a measure of the occupancies of sites M1 and M2 of postspinel Mn_2FeO_4 at 18 GPa. The outer doublet has a larger quadruple splitting and a much lower intensity than the inner doublet.

Mössbauer spectroscopic study confirmed the cation distribution in the postspinel structure as:

$$^{VIII}\left(Mn^{2+}_{1-d}\ Fe^{2+}_{d}\right)\ ^{VI}\left[Mn^{3+}_{1-d}\ Fe^{3+}_{1-d}\right]O_4$$

M1 site M2 site

(where the superscripts VI and VIII indicate the coordination numbers).

In the case of spinel, the outer sextet spectral feature indicates Fe^{3+} at the tetrahedral sites, while the inner sextet arises from a combination of Fe^{2+} and Fe^{3+} at the octahedral sites of both spinels. The site occupancies indicated by x in $Mn_{3-x}Fe_xO_4$ change with pressure. The magnetic and electric characters of these compounds are defined by the cation distributions. The cation distribution is consistent with the structural analysis by neutron diffraction study. The postspinel phase shows no hyperfine structure in its spectrum, proving that it is paramagnetic.

The hypothetical total magnetic moment under ambient conditions can be evaluated from the combination of the preference of Mn^{3+} for octahedral sites and the site occupancy determined by X-ray Mössbauer and neutron diffraction studies. The site occupancies are presented in Table 1.

Diffraction study confirmed the spinel structure. The observed Mössbauer intensities provide sufficient proof of two hyperfine structures, although the background intensities are rather large. The observed peak positions and intensities are sufficiently clear to discuss the interest here in the pressure enhancement of electrical conductivity from semiconductor to metal in $Mn_{3-x}Fe_xO_4$ spinel and postspinel. We

Table 1
The magnetic moment and site occupancy at the A and B site of tetragonal Mn_2FeO_4 spinel.

Press(GPa)	Lattice constant		Vol (Å^3)	site occupancy		magnetic moment		total	χ^2	R(F^2)
	a (Å)	c (Å)		Mn(tet)	Mn(oct)	A(tet)	B(oct)			
0.0001	5.9453	8.7844	310.98	0.902	0.548	−2.002	4.655	2.653	2.173	0.222
2.2	5.9466	8.7498	309.41	0.916	0.542	−1.186	3.314	2.128	2.957	0.167
4.0	5.9392	8.6494	305.10	0.934 0.533	−0.077	2.043	1.966	3.866	0.178	
6.4	5.9232	8.5094	301.39	0.964	0.524	−1.556	3.166	1.610	3.099	0.139
10.0	5.9106	8.4167	294.69	0.962	0.519	−2.003	3.381	1.378	6.239	0.211
13.4	5.9246	8.3986	292.09	0.987	0.507	−1.423	2.968	1.545	3.768	0.178

Table 1 Site occupancy and magnetic moment at the A and B site of tetragonal Mn_2FeO_4 spinel. Ferrimagnetic magnetic moments of individual A and B site are shown. The moment in the unit cell is presented in total.

have discussed in more detail the effects of pressure on IS, QS, and B_{IF} in another submitted paper.

3.3. Pressure dependences of the electrical resistivities of Mn_2FeO_4 and $MnFe_2O_4$

We measured the electrical resistivities of $MnFe_2O_4$ (cubic ferrimagnetic) and Mn_2FeO_4 (tetragonal ferrimagnetic) under high pressure. Both samples are semiconductors, in which electron mobility μ is related to the conduction. Holes can move through a semiconductor crystal lattice as electrons can, and act similarly to positively charged particles. If an electron is excited to a higher state, it leaves behind a hole.

Electric conduction rate σ is derived from the electron mobility μ: $\sigma = q\mu$ (where q is electric charge).

Current I is derived as a function of carrier mobility μ and applied electric field E:

$$I=\sigma AE=en\mu AE \tag{7}$$

Generally, μ depends on temperature T, the applied electric field E, and the concentration of localized states N. Carrier mobility strongly depends on the concentration of localized states. In the case of nearest-neighbor hopping, the following expression can be fitted to the experimental results:

$$\mu = exp(-2/\lambda N_o^{1/3}) \tag{8}$$

where N_o is the concentration and λ is the localization length of the localized states. This equation is characteristic of incoherent hopping transport, where the limiting factor is the exponential decay of hopping probability with inter-site distance.

Electron mobility μ is expressed by electric field V/λ, where λ is the distance between particles with electrons. Electron mobility is given by:

$$\mu = V/\lambda\ e \tag{9}$$

Note that μ has a thermal dependency. The present experiment was, however, conducted at constant temperature. The electron mobilities of Fe^{2+} and Fe^{3+} under compression are affected by the variable λ. Besides the charge transport under pressure, the compressibility of the cation sites has to be discussed in relation to the pressure dependence of electrical resistivity.

Electronic charge distributions of Fe^{2+} and Fe^{3+} were also assessed by X-ray Mössbauer experiments under high-pressure conditions at SPring-8 [29]. The resistivities of Mn_2FeO_4 and $MnFe_2O_4$ decrease markedly on increasing the pressure from ambient to about 14 GPa and 18 GPa, respectively (Fig. 4). That of $MnFe_2O_4$ slightly increases between 20 and 24 GPa. In this region, the two-phase mixture of spinel and postspinel is observed. However, it decreases on approaching the highest studied pressure of 40 GPa in the postspinel region. The resistivity indicates that electron hopping persists as the mechanism of charge transport through the transition from spinel to postspinel phase. The resistivity of the postspinel phase in the high-pressure region decreases to within an order of magnitude of metallic values.

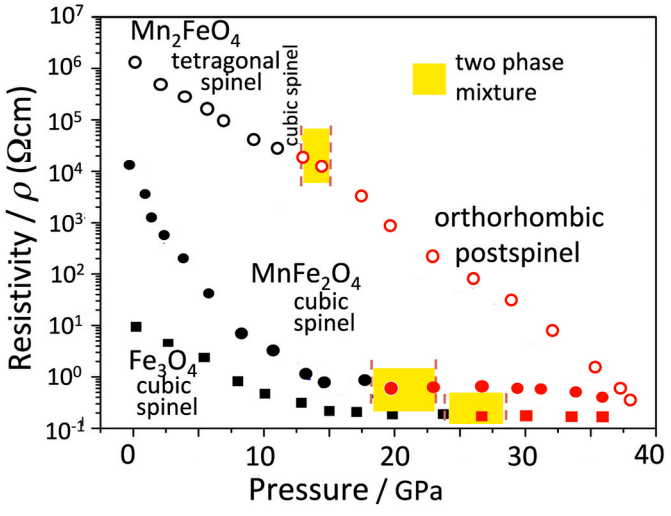

Fig. 4. Pressure dependences of the electrical resistivities of $MnFe_2O_4$ and Mn_2FeO_4. The resistivity of the spinel phase varies enormously with pressure. Postspinel shows extremely low resistivity, akin to metallic character. The pressure dependence of Fe_3O_4 is taken from Muramatsu et al. [13].

The electrical resistivity of cubic $MnFe_2O_4$ spinel at ambient temperature decreases from $\rho = 10^{4.1}$ Ω·cm to $\rho = 10^{0.0}$ Ω cm, and that of tetragonal spinel Mn_2FeO_4 decreases from $\rho = 10^7$ Ω·cm to $\rho = 10^1$ Ω cm. The latter shows a much higher resistivity than the former. These spinels have insulating character under ambient pressure. Both show enhanced hopping conduction probability between Fe^{2+} and Fe^{3+} ions with increasing pressure. However, during decompression and compression, resistivity shows a different curve as shown in Supplementary Fig. 3.

At even higher pressures, the resistivity decreases monotonously. The postspinel phase shows resistivity two orders of magnitude lower than that of the spinel during the compression process. The electrical resistivity of postspinel $MnFe_2O_4$ at ambient temperature decreases from $\rho = 10^{0.0}$ Ω cm at 18 GPa to $\rho = 10^{-2.0}$ Ω cm at 40 GPa. The lowest resistivity is akin to metallic character.

The probability Γ_{ij} of electron hopping between i and j with different localized energy levels is represented by the following function:

$$\Gamma_{ij} \propto exp\ (-2r_{ij}/a - E_{ij}/k_BT) \tag{10}$$

where a is the localized energy level length, r_{ij} is the distance between i and j, E_i and E_j are the localized energies, k_B is the Boltzmann constant, and T is the absolute temperature. The energy difference between E_i and E_j is $E_{ij} = |E_i - E_j|$. The present electrical resistivity measurements were performed under variable pressures at constant temperature.

In the structure change under compression, the A-O, B–O bond lengths, and A-O-B bond angles are defended.

Electron-hopping conduction involves electrons of the cations at the A and B sites.

The inter-cation distance changes of A-A, A-B, and B–B in $MnFe_2O_4$ and Mn_2FeO_4 spinels and of M1-M1, M1-M2, and M2-M2 in the postspinel upon compression at high pressure are presented in Supplementary Table 1, 2, and 3. These interatomic distances in $MnFe_2O_4$ and Mn_2FeO_4 are illustrated in Fig. 5. The B–B distance is much smaller than the A-A and A-B distances. Super-exchange between adjacent B cations thus facilitates extremely low resistivity. Under compression, the shorter B–B distance promotes higher conduction. Supplementary Fig. 4 shows the B–B super-exchange model in relation to corner-sharing octahedra.

It is known that electrical conduction is the movement of electrically charged particles through a transmissive medium. Electrical resistivity mainly relates to hole conduction, band-gap conduction, and electron-hopping conduction. The present experiments on the pressure dependence of B–B bond distance and the site occupancy change of mixed-charge cations and the Mössbauer spectra indicating the distribution of Fe^{2+} and Fe^{3+} at the A and B sites of the spinel structure are consistent with electron-hopping conduction under compression. These phenomenological observations indicate lattice deformation and charge transfer. However, polaron hopping conduction may also be possible. Metallization in the postspinel under extreme high-pressure conditions due to band conduction, as implied by first-principles calculations, is discussed in the following section.

The pressure dependence of the resistivity of Mn_2FeO_4 is much more marked than that for $MnFe_2O_4$. Equations of state for $Mn_{3-x}Fe_xO_4$ spinel solid solutions were calculated from the third-order Birch–Murnaghan isothermal equation of state:

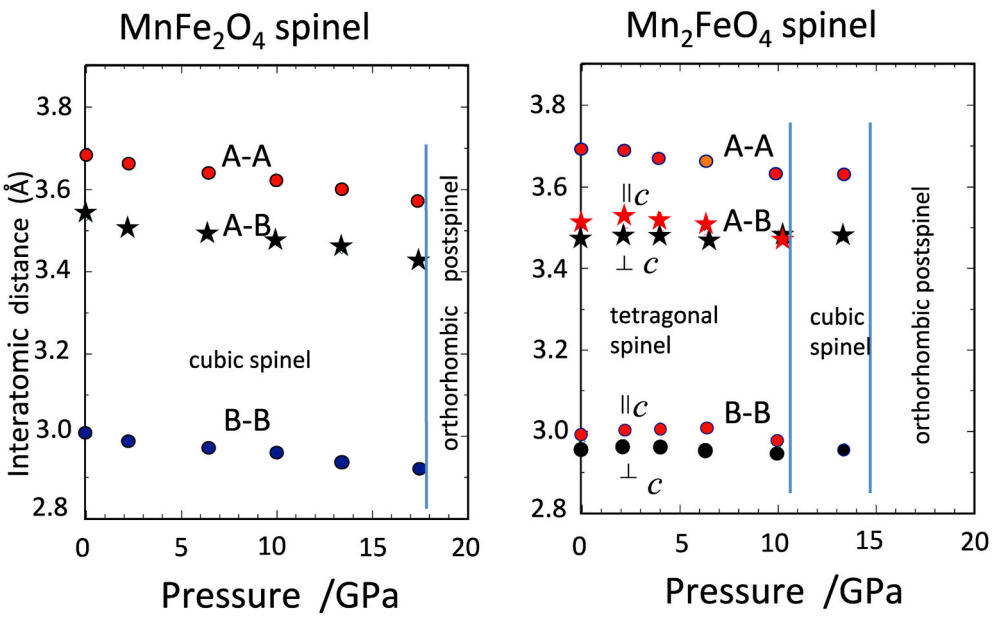

Fig. 5. Inter-cation distances A-A, B–B, and A-B in $MnFe_2O_4$ and Mn_2FeO_4. The B–B distances in $MnFe_2O_4$ and Mn_2FeO_4 are much shorter than the A-A and A-B distances.

$$P(V) = \frac{3B_o}{2}\left[(V_o/V)^{7/3} - (V_o/V)^{5/3}\right]\left\{1 + \frac{3}{4}\left(B_o' - 4\right)\left[(V_o/V)^{2/3} - 1\right]\right\} \quad (11)$$

where P is the pressure, V_0 is the reference volume, V is the deformed volume, B_0 is the bulk modulus, and B_0' is the derivative of the bulk modulus with respect to pressure.

The bulk modulus and its derivative are usually obtained from fits to experimental data and are defined as:

$$B_o = -V\left(\partial P/\partial V\right)_{P=0} \text{ and } B_o' = \left(\partial B/\partial P\right)_{P=0} \quad (12)$$

The B_o and B_o' of Mn_2FeO_4 and $MnFe_2O_4$ were determined as follows:

$MnFe_2O_4$ B_o = 155.8(8) GPa B_o' = 4.9(1.1) cubic spinel

Mn_2FeO_4 B_o = 104.2(3) GPa B_o' = 3.9(0.7) tetragonal spinel

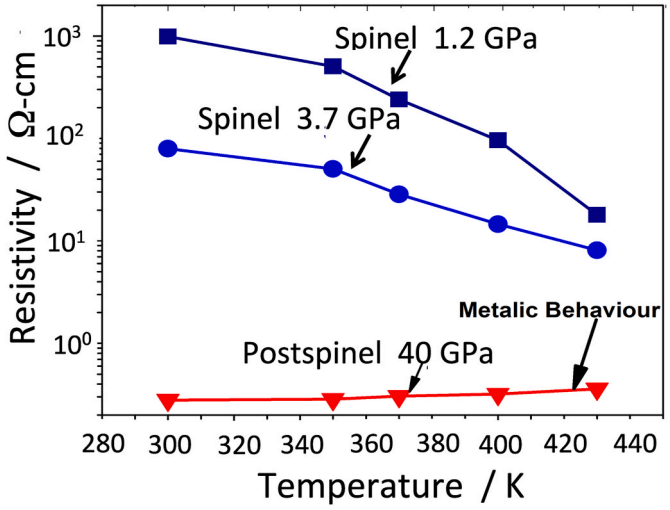

Fig. 6. Temperature dependence of the electrical resistivity of Mn_2FeO_4 at high pressure. The spinel phases at 1.2 GPa and 3.7 GPa display semiconductor behavior, whereas the postspinel phase at 40 GPa presents metallic character.

The metallization pressure from the semiconductor state decreases with increasing Mn content in $Mn_{3-x}Fe_xO_4$. Fe_3O_4 has B_o = 172 GPa, B_o' = 4 (fixed) [36].

The two spinels show almost the same contraction with increasing pressure, as shown in Supplementary Tables 1 and 2 However, the significant difference in resistivity between these spinels may be attributed to electron mobility according to Eq (9). The occupancies of Fe^{2+} and Fe^{3+} at the B sites of $MnFe_2O_4$ are much higher than in the case of Mn_2FeO_4.

Dimers assembled from the linking of octahedral sites extend in two directions parallel to the *x*- and *y*-axes. Electron hopping is much more extensive than in the spinel structure. Furthermore, compression of the octahedra at high pressure favors two-dimensional planar conduction due to the shortened inter-cation distances.

The temperature dependence of resistivity (Fig. 6) shows that the Mn_2FeO_4 spinel phase is a semiconductor, whereas the postspinel phase is metallic-like at extremely high pressures. The resistivity of the postspinel at 35 GPa increases with increasing temperature up to 440 K. The octahedral Mn_2O_{10} dimer in the postspinel structure is noticeably distorted by compression, as shown in Supplementary Table 3. The electronic spin state indicates the distortion by Fe^{2+} ($3\ d^5$) under high pressure. The octahedral B–B inter-cation distance in the Mn_2FeO_4 spinel structure (2.962 Å at 13.4 GPa) implies strong electron hopping. On the other hand, the M2-M2 interatomic distance of the octahedral sites in Mn_2FeO_4 postspinel (2.642 Å at 26.8 GPa, as shown in Supplementary Table 3) is much shorter than the B–B distance. This short distance may lead to low resistivity through spin transition or a change in band structure. A three-dimensional array of octahedral Mn_2O_{10} dimers in the postspinel enhances the conductivity from semiconductor-like to metallic-like.

The distortion enlarges the 10 Dq between the *e* and *t* orbitals, but the degeneracy widens the splitting of the energy levels between (d_x2-$_y2$) and (d_z2) in the *e* orbitals of Fe^{2+} and Fe^{3+}. The electronic band thus becomes smaller between *e* and *t*. In our previous X-ray emission study (XES) of the high-pressure structure transition of Fe_2TiO_4 [37], the electronic spin transition was found to commence at about 14 GPa. This is very similar to the pressure of the structural transition to postspinel at 15 GPa observed by XRD. The XRD and XES experiments indicated three transitions of Fe_2TiO_4, which reflected the electronic spin states in the high-spin (HS)-to-low-spin (LS) transition of Fe^{2+} in the octahedral site.

The extremely low resistivity of the postspinel phase above 24 GPa may be induced by an HS-to-LS spin-crossover transition of Fe^{2+} and Fe^{3+} at the octahedral M2 sites.

Site occupancy (Supplementary Table 3) of the postspinel phase of Mn_2FeO_4 varies with increasing pressure. The postspinel phase is not reversible and then the phase quenched from 35 GPa clarifies the structure under ambient conditions: a highly ordered structure with an ideal cation distribution, $^{M1}(Mn)^{M2}[Mn.Fe]O_4$.

3.4. Theoretical calculation of density of state

We calculated the density of state (DOS) to confirm the electronic correlation in the postspinel at high pressures. We applied a combined approach of density functional theory (DFT) and dynamical mean field theory (DMFT) for Mn_2FeO_4 postspinel based on the structure at 26.8 GPa. We used the Rutgers DFT + embedded DMFT functional code [38] combined with the WIEN2k code, which uses the full-potential augmented plane-wave method [39]. The Perdew–Burke–Ernzerhof generalized gradient approximation (GGA) was used for the exchange correlation functional [40]. The correlation effect of the Mn d and Fe d orbitals was treated by a DMFT loop on top of an effective one-electron Hamiltonian generated by WIEN2k calculation.

A continuous time quantum Monte Carlo (CTQMC) impurity solver was used to solve the auxiliary quantum impurity problem. Coulomb interaction parameters of $U = 10$ eV and $J = 1$ eV were used for both Mn and Fe d orbitals. To simplify the calculation, we assumed that the M1 sites were mainly occupied by Mn atoms and that the M2 sites were occupied by both Mn and Fe atoms.

Fig. 7 shows the *k*-resolved spectral function and DOS of postspinel Mn_2FeO_4 at 300 K. Although the spectral function is very incoherent due to the electronic correlation effect of d orbitals, it clearly shows metallic behavior.

In the strongly electron-correlated system, the bandwidth is renormalized in comparison with the conventional DFT result, since DFT cannot adequately describe the electron correlation effect. As the correlation strength increases, the quasi-particle bandwidth decreases. The degree of renormalization can be quantified by the quasi-particle weight Z, which is the inverse of the effective mass m*/m. The Mn d orbitals are much more strongly renormalized than the Fe d orbitals, as shown by the DOS. For more quantitative analysis, the mass enhancement (m*/m) was calculated from the DMFT self-energy. The mass enhancement of Mn d orbitals is six times larger than that of Fe d orbitals (m*/m Fe ≈ 16.81, m*/m Mn ≈ 2.67). At the critical point, the effective mass m*/m diverges and the spectral weight near the Fermi level disappears (the system becomes a Mott insulator). Therefore, the degree of renormalization is a good indicator of how close the system is to the Mott insulating phase. DFT + DMFT can suitably describe the electron correlation effect. DFT + DMFT band dispersion can be represented by the scaling relationship near the Fermi level – $\in_{DMFT}(k) = \in_{DFT}(k)/(m^*/m)$. In the DOS from DFT + DMFT calculations, the Mn d bands are more strongly renormalized compared to the Fe d bands. This indicates the strong electron correlation effect in Mn d orbitals, indicating that the Mn site (M1 site) is close to the Mott insulating state (Mn d bands can easily form a gap, depending on external conditions, such as pressure or doping).

This significant difference arises from the local environments of each metal site. The Mn and Fe (M2 site)-O bond lengths are much smaller than the Mn (M1 site)-O bond lengths. Due to the greater p-d hybridization at the M2 sites, the Fe d orbitals are weakly correlated. These weakly correlated M2 sites are far from the Mott insulating state. Consequently, we can guarantee metallic behavior of postspinel Mn_2FeO_4 under high pressure.

Our experiments have revealed extremely low electrical resistivity, of the same order as that of metals, in both $MnFe_2O_4$ and Mn_2FeO_4 postspinels under high pressure, and band conduction accounts for the metallization under such extreme conditions. In the present study, we performed a DOS calculation of the metallization of Mn_2FeO_4 at 26.8 GPa. We have prepared **Supplementary Information File 3** for a more detailed derivation of the first-principles calculation.

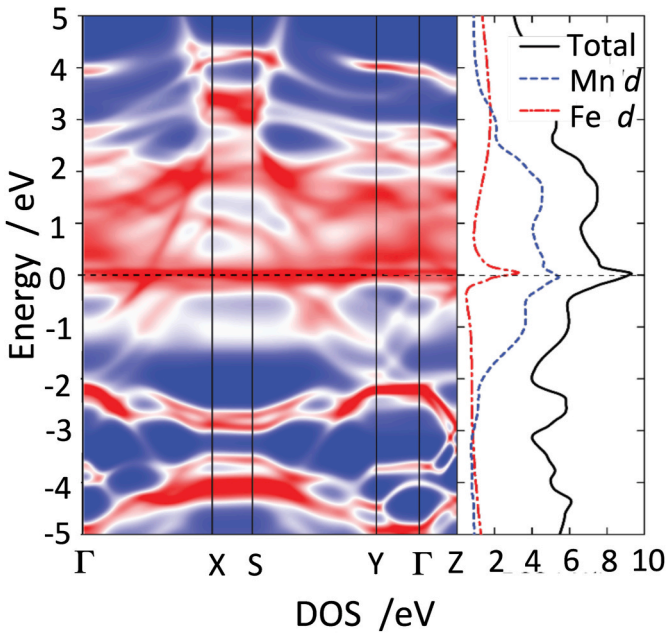

Fig. 7. The *k*-resolved spectral function and density of states of Mn_2FeO_4 at 26.8 GPa. The spectral function is very incoherent due to the electronic correlation effect of d orbitals. The metallic character is clearly evident.

4. Conclusion

The cation site occupancy changes and magnetic structures in $Mn_{3-x}Fe_xO_4$ spinel have been investigated by neutron time-of-flight (TOF) scattering under high-pressure conditions at J-PARC and by synchrotron X-ray Mössbauer experiments at SPring-8. $Mn_{3-x}Fe_xO_4$ spinel is a ferrite compound with mixed-charge cations of Mn^{2+}, Mn^{3+}, Fe^{2+}, and Fe^{3+} at tetrahedral and octahedral sites. Neutron diffraction study has revealed the precise structure, based on the significant difference in coherent diffraction scattering lengths of Mn (−3.73 fm) and Fe (9.54 fm). The integrated intensity I_o of neutron diffraction is produced by a combination of magnetic scattering factor and nuclear scattering factor: $I_o = s(\boldsymbol{h})A(\boldsymbol{h})L(\boldsymbol{h})m(\boldsymbol{h})\{|F_N(\boldsymbol{h})|^2 + |F_M(\boldsymbol{h})|^2\}$. Our neutron diffraction study and X-ray Mössbauer spectroscopic study have confirmed the cation distribution.

The B–B distance is much smaller than the A-A and A-B distances. Super-exchange between adjacent B cations is thus associated with extremely low resistivity. The resistivity indicates that electron hopping persists as the mechanism of charge transport through the transition from spinel to postspinel. The resistivity of the postspinel in the high-pressure region is within an order of magnitude of metallic values. The pressure dependence of the resistivity of Mn_2FeO_4 is much stronger than that of $MnFe_2O_4$.

The pressure–enhancement to metal relationship in $Mn_{3-x}Fe_xO_4$ postspinel has been revealed by electrical resistivity measurements. Besides our electrical resistivity measurements and neutron and X-ray Mössbauer experiments, functional theoretical calculations have indicated that the spectral function is very incoherent due to the electronic correlation effect of d orbitals, but it clearly shows metallic behavior. Theoretical approaches to show densities of state (DOS) have been used to elucidate the electrical properties of these manganese ferrites. To verify the metallic behavior of post-spinel Mn_2FeO_4 under high pressure, we applied a combined approach of density functional theory (DFT) and dynamical mean field theory (DMFT) at 26.8 GPa. Functional theoretical calculation clearly indicated metallic behavior at high pressure. Fe

d orbitals are more strongly renormalized than Mn d orbitals.

Role of the funding source

This research did not receive any specific grant from funding agencies in the public, commercial, or not-for-profit sectors.

Declaration of competing interest

The authors declare that they have no known competing financial interests or personal relationships that could have appeared to influence the work reported in this paper.

Acknowledgements

We would like to express our great thanks to Prof. Yukio Noda of the Institute of Multidisciplinary Research for Advanced Materials, Tohoku University, Japan, for fruitful discussions. Our investigation was performed under J-PARC Proposal No. 2016B0018. We also appreciate access to facilities for X-ray Mössbauer spectroscopic study at SPring-8 BL-10XU supported by Proposal No. 2018A1088.

Appendix A. Supplementary data

Supplementary data to this article can be found online at https://doi.org/10.1016/j.jpcs.2022.110721.

References

[1] Y. Yafet, C. Kittel, Phys. Rev. 87 (1952) 290.
[2] B. Boucher, R. Buhl, M. Perrin, J. Appl. Phys. 42 (1971) 1615.
[3] J. Gutzmer, N.J. Beukes, A.S. Kleyenstuberanda, E. Burger, Mineral. Mag. 59 (1995) 703.
[4] J.M. Hastings, L.M. Corlis, Phys. Rev. 104 (1956) 328.
[5] P.A. Murasik, G. Roult, J. Phys. 25 (1964) 522.
[6] Y. Fei, H.K. Mao, R. Hemley, J.F. Shu, G. Shen, Am. Mineral. 84 (1999) 203.
[7] C. Haavik, S. Tolen, H. Fjellvag, M. Hanfland, D. Hauserman, Am. Mineral. 85 (2000) 514.
[8] A. Kuriki, Y. Moritomo, Y. Ohishi, K. Kato, E. Nishibori, M. Takata, M. Sakata, N. Hamada, S. Todo, N. Mori, O. Shimomura, A. Nakamura, J. Phys. Soc. Jpn. 71 (2002) 3092.
[9] L.S. Dubrobinsky, N.A. Dubrovinskaia, C. McCammon, G.K. Rozenberg, R. Ahuja, J. M. Osorio-Guillen, V. Dmitriev, H.P. Weber, T.L. Bihan, B. Johansson, J. Phys. Condens. Matter 15 (2003) 7697.
[10] G.K. Rozenberg, Y. Amiel, W.M. Xu, M.P. Pasternak, R. Jeanloz, M. Hanfland, R. D. Taylor, Phys. Rev. B 75 (2007), 020102.
[11] H.J. Reichmann, S.D. Jacobsen, Am. Mineral. 89 (2004) 1061–1066.
[12] S. Todo, N. Takeshita, T. Kanehara, T. Mori, N. Mori, J. Appl. Phys. 89 (2001) 7347.
[13] T. Muramatsu, L.V. Gasparov, H. Berger, R. Hemley, V.V. Struzhkin, J. Appl. Phys. 119 (2016), 135903.
[14] L. Ye, S. Zhai, X. Wu, C. Xu, K. Yang, Y. Higo, Phys. Chem. Miner. 42 (2015) 569.
[15] C.R. Paris, H. Olijnyk, Eur. J. Mineral 4 (1992) 87.
[16] Y. Zhang, H. Yan, Q. Song, Q. Zhou, Z. Li, Y. Liu, J. Alloys Compd. 818 (2020), 152881.
[17] S. Rahman, S. Sudeshna, D. Errandonea, Y. Shuai, Y. Ke, L. Junling, W. Lin, Phys. Rev. B 95 (2017), 024107.
[18] S. Rahman, H. Saquib, J. Zhang, D. Erradonea, C. Menendez, C. Cazorla, S. Samanta, X. Li, J. Lu, L. Wang, Phys. Rev. B 97 (2018), 174102.
[19] H.J. Van Hook, M.L. Keith, Am. Mineral. 43 (1958) 69.
[20] H.F. McMurdie, B.M. Sullivan, F.A. Mauer, Res. Pap. SO **45** (1959), RP2111.
[21] M. Miyamoto, T. Mikouchi, Geochem. Cosmochim. Acta 60 (1996) 2917.
[22] H.K. Mao, J. Xu, P.M. Bell, J. Geophys. Res. 91 (1986) 4673.
[23] A.P. Hammersley, Fit2D V12012 Reference Manual V 6.0, ESRF, 2004.
[24] F. Izumi, T. Ikeda, European Powder Diffraction, Mater. Sci. Forum 198 (2000).
[25] T. Hattori, F.A. Sano-Furukawa, K. Komatsu, A. Yamada, Y. Inamura, T. Nakatani, Y. Seto, T. Nagai, W. Utsumi, T. Iitaka, H. Kagi, Y. Katayama, T. Inoue, T. Otomo, K. Suzuya, T. Kamiyama, M. Arai, T. Yagi, Nucl. Instrum. Methods Phys. Res. 780 (2015) 55.
[26] A. Sano-Furukawa, T. Hattori, H. Arima, A. Yamada, S. Tabata, M. Kondo, A. Nakamura, H. Kagi, T. Yagi, Rev. Sci. Instrum. 85 (2014), 113905.
[27] A.C. Larson, R.B. Von Dreele, *General Structure Analysis System (GSAS)*, Los Alamos National Laboratory Report LAUR 86, 1994, p. 748.
[28] B.H. Toby, EXPGUI, a graphical user interface for GSAS, J. Appl. Crystallogr. 34 (2001) 210–213.
[29] N. Hirao, S.I. Kawaguchi, K. Hirosae K. Shimizu, E. Ohtani, Y. Ohishi, Matter Radiat. Extrem. 5 (2019), 018403.
[30] J.M. Hastings, L.M. Corliss, Phys. Rev. 104 (1956) 328.
[31] K. Kleinstück, E. Wieser, P. Kleinnert, R. Perthel, Phys. Status Solidi 8 (1965) 271.
[32] C. Prescher, C. McCammon, L. Dubrovinsky, Appl. Crystallogr. 45 (2012) 329–331.
[33] L. Ye, S. Zhai, X. Wu, C. Xu, K. Yang, Y. Higo, Phys. Chem. Miner. 42 (2015) 569–577.
[34] L. Malavasi, C. Tealdi, M. Amboage, M.C. Mozzatti, G. Flor, Physiol. Res. B 238 (2005) 171.
[35] T. Yamanaka, A. Uchida, Y. Nakamoto, Am. Mineral. 93 (2008) 1874.
[36] A. Ricolleau, Y. Fei, Am. Mineral. 101 (2016) 719–725.
[37] T. Yamanaka, A. Kyono, Y. Nakamoto, Y. Meng, S. Kharlamova, V.V. Struzhkin, H. K. Mao, Am. Mineral. 98 (2013) 736.
[38] K. Haule, C.H. Yee, K. Kim, Phys. Rev. B 81 (2010), 195107.
[39] P. Blaha, K. Schwarz, G.K.H. Madsen, D. Kvasnicka, J. Luitz, R. Laskowski, F. Tran, L.D. Marks, WIEN2k, *An Augmented Plane Wave+Local Orbitals Program for Calculating Crystal Properties* (Karlheinz Schwarz, Techn, Universität Wien, Austria, 2018.
[40] J.P. Perdew, K. Burke, M. Ernzerhof, Phys. Rev. Lett. 78 (1997) 1396.